Article

Elongation factor Tu promotes the onset of periodontitis through mediating bacteria adhesion

Check for updates

Leyi Xiao[1,4], Yingying Pu[1,2,4], Yu Cui[1,4], Chen Chen[1], Qi Xiao[1], Yulan Wang[1], Yan Wei[1], Mengge Feng[1], Tiange Zhang[1], Shanyi Yang[1], Jingxuan Zhou[1], Yueqi Ni[1], Jinglun Zhang[1], Hebin Liao[2], Jingwen Wu[1] & Yufeng Zhang[1,2,3] ✉

Periodontitis, a leading cause of adult tooth loss and linked to various systemic diseases, is promoted by subgingival plaque biofilms, with *Streptococci* as early colonizers responsible for surface adhesion. Current studies of *Streptococci* adhesion have focused on bacteria surface adhesins with acquired protein membranes on the tooth surface, yet no critical proteins with implications for the overall early adhesion of subgingival plaque have been reported. Here, we identified that the "Barrel-like adhesion domain" of streptococcal EF-Tu facilitates cell-surface attachment, promotes biofilm formation, and contributes to the development of periodontitis. In the adherent state, EF-Tu is transported from the cytoplasm to the cell surface through membrane vesicles. Furthermore, we first found that simeprevir, an FDA-approved drug, binds to the "Barrel-like adhesion domain" of EF-Tu and effectively inhibits the protein's surface adhesion and secretory pathways. Simeprevir showed the ability to inhibit dental plaque formation and provided prevention and treatments for periodontitis.

Periodontitis is a highly prevalent chronic disease worldwide, affecting ~20–50% of the global population[1,2]. This condition progressively compromises the integrity of the tissues supporting the teeth, ultimately leading to tooth loss. Moreover, epidemiological studies have linked periodontitis to various systemic diseases, including cardiovascular disease, rheumatoid arthritis, diabetes, nonalcoholic fatty liver disease, Alzheimer's disease, inflammatory bowel disease, and certain cancers[3–10]. The main etiology of periodontitis is the formation of subgingival bacterial biofilms and dysbiosis of the microbial community[11]. Existing treatments for periodontitis focus on mechanical removal of subgingival plaque biofilms[12], however, recolonization of bacteria still occurs, leading to a recurrence of periodontitis[13]. Not only is subgingival plaque resistant to antimicrobial medications and difficult to remove by the immune system, but it also triggers a sustained periodontal inflammatory response that can further lead to periodontal tissue damage. Hence, it is imperative to elucidate the mechanisms underlying the formation of subgingival plaque biofilm, with a view toward advancing future strategies for the treatment and prevention of periodontitis.

Gram-positive bacteria *Streptococci* serve as major early colonizers of subgingival plaque biofilms, whose adherence is crucial for the temporal and spatial development of the complex bacterial communities in the gingival crevice. Early colonized *Streptococci* can serve as co-pathogens to promote adhesion of the causative bacterium, *Fusobacterium nucleatum* (*F. nucleatum*), to form biofilms with the development of periodontitis[14,15]. *F. nucleatum* co-aggregates with late-stage colonizers, such as *Porphyromonas gingivalis* (*P. gingivalis*), to promote subgingival plaque maturation and pathogenicity[16–19]. *Streptococci* co-aggregate with the pathogenic bacterium *P. gingivalis*, enhancing colonization of both. This is thought to be the initial event in oral infection by *P. gingivalis*[20]. In addition to physical colonization, *Streptococci* produce metabolites that regulate the microecological balance of the subgingival plaque. They are also the most proficient oral bacterial producers of bacteriocins, which help them to select their "colonization neighbors", promote the establishment of communities of specific bacterial species, and influence the ecological balance of the oral ecosystem[21,22]. Therefore, to control subgingival plaque formation and modulate biofilm pathogenicity, the adhesion mechanism of *Streptococci* becomes a critical issue.

Current studies on the adhesion mechanism of *Streptococci* suggest that adhesins, particularly the Antigen (Ag) I/II polypeptides, play a crucial role in mediating biofilm formation by adhering to protein substrates in the

[1]State Key Laboratory of Oral & Maxillofacial Reconstruction and Regeneration, Key Laboratory of Oral Biomedicine Ministry of Education, Hubei Key Laboratory of Stomatology, School & Hospital of Stomatology, Wuhan University, Wuhan University, 430079 Wuhan, China. [2]Medical Research Institute School of Medicine Wuhan University, 430071 Wuhan, China. [3]TaiKang Center for Life and Medical Sciences, Wuhan University, 430071 Wuhan, China. [4]These authors contributed equally: Leyi Xiao, Yingying Pu, Yu Cui. ✉e-mail: zyf@whu.edu.cn

acquired pellicles[23]. GspB and Hsa are serine-rich repeat (Srr) glycoproteins that mediate the binding of *S. gordonii* to human salivary mucin and platelet glycoproteins in acquired pellicles[24]. However, the Srr structure is not present in *Streptococcus mutans* (*S. mutans*), which adheres to the tooth surface via glucosyltransferases[25,26]. Adhesin-mediated colonization tends to be species-specific, and no generalized adhesion proteins have been reported for the initial adhesion of *Streptococci*. Therefore, it is challenging to achieve significant therapeutic effects by targeting species-specific adhesion proteins because the plaque biofilm is a complex microecosystem.

This study identified EF-Tu as a potential adhesion protein through high-throughput protein mass spectrometry analysis of clinical plaques. EF-Tu is a protein translation elongation factor that catalyzes the binding of aminoacyl-tRNA to the A-site of the ribosome inside living cells, which is conserved in *Streptococci*. Additionally, EF-Tu can be secreted to the bacterial surface, acting as a moonlighting protein[27,28]. It stimulates the host's immune response and mediates adhesion and invasion of host cells[29–31]. In addition, it can bind MreB and modulate bacterial shape[32,33]. However, the role of EF-Tu in periodontitis has not been reported yet, and its moonlighting functions and secretory mechanisms of EF-Tu in biofilms are not clear. In addition, the functional domain of the protein as a moonlighting protein has not been identified yet.

Here, we discovered that the translational elongation factor EF-Tu of *Streptococci* is secreted to the bacterial cell surface and plays a crucial role in cell-surface attachment, promoting the development of subgingival plaque biofilms. Furthermore, we performed virtual drug screening targeting the structure of the EF-Tu protein and experimental validation to identify that simeprevir, an FDA-approved macrocyclic compound, can inhibit EF-Tu adhesion activity and provide therapeutic strategies for prevention and supplementary treatments for periodontitis.

Results

Streptococci EF-Tu is secreted extracellularly in periodontitis patients' subgingival plaque

To investigate whether secreted proteins contribute to the dental surface adhesion of oral microbiota, we collected bacterial secretomes from the saliva and subgingival plaque of healthy individuals and patients with periodontitis. The samples were subjected to mass spectrometry (MS) analysis. Remarkably, the MS analysis showed significant enrichment of *Streptococci* EF-Tu, a translational elongation factor responsible for catalyzing the binding of an aminoacyl-tRNA (aa-tRNA) to the ribosome, in the secretome of subgingival plaque from periodontitis patients (Fig. 1a and Supplementary Fig. 1a). *Streptococci* are known to be early colonizers of subgingival plaque biofilm and play a key role in periodontitis pathogenesis[34]. Our metagenomic sequencing analysis revealed that *S. oralis*, *S. gordonii*, and *S. sanguinis* are the main *Streptococci* species enriched in subgingival plaque biofilms from periodontitis patients (Fig. 1b and Supplementary Fig. 1b–f). To investigate the roles of EF-Tu in biofilm development, we selected *S. oralis* as the model organism. Bacterial surface proteomic analysis of *S. oralis* showed a remarkable 4.4-fold enrichment of EF-Tu in the secretome of the adhesion state compared to that of the planktonic state (Fig. 1c). These results demonstrate that EF-Tu of *Streptococci* is secreted out of the adhesion bacteria, indicating its potential role in promoting biofilm formation and periodontitis progression.

Secreted EF-Tu promotes biofilm development and periodontitis onset

To further investigate whether EF-Tu contributes to biofilm formation, we generated the EF-Tu knockout mutant (Δ*tuf*), the EF-Tu overexpression strain (pDL278*tuf*), and the rescued strain (pDL278*tuf*Δ*tuf*) to assess their biofilm formation capacity. We first tested the growth curves of these four bacteria and found that knockout of the *tuf* gene had no significant effect on the growth of *S. oralis* (Supplementary Fig. 1i). We then evaluated the extent of biofilm formation over time by crystal violet staining. Remarkably, the results showed the Δ*tuf* strain formed the fewest biofilms over time, while the rescued strain pDL278*tuf*Δ*tuf* displayed a similar level of biofilm

formation as the WT strain. On the other hand, the overexpression strain pDL278*tuf* formed the most abundant biofilms (Fig. 1d and Supplementary Fig. 1g, h). These findings were further confirmed by scanning electron microscopy (SEM) analysis (Fig. 1e). These results strongly suggest that bacterial cell surface EF-Tu plays a critical role in biofilm formation.

To investigate the impact of *Streptococci* EF-Tu on the progression of periodontitis, we established a periodontitis mouse model by ligating the bilateral maxillary second molars of the mice and daily dropping on the ligature with *S. oralis* strains for five consecutive days (Fig. 1f). Using micro-computed tomography (Micro-CT) analysis, we examined the maxillary alveolar bone and observed that the group infected with Δ*tuf* strain had the least amount of bone resorption among the infected groups (Fig. 1g). Additionally, this group exhibited higher values for trabecular number (Tb. N) and trabecular bone volume per tissue volume (BV/TV) compared to the *pDL278tuf*Δ*tuf*-infected and WT-infected groups (Fig. 1h, i). These results suggest that knockout of the *tuf* gene effectively inhibited bone resorption in the alveolar bone. Furthermore, we performed histological analyses of the alveolar bone tissue using hematoxylin–eosin (HE) staining and tartrate-resistant acid phosphatase (TRAP) staining (Fig. 1j, k). The results showed that the levels of cementoenamel junction to alveolar bone crest (CEJ-ABC) distances and osteoclast infiltration in the Δ*tuf*-infected group were close to mock control and significantly lower than those in the WT-infected group (Fig. 1l, m). Moreover, immunofluorescence staining of macrophages and neutrophils in alveolar bone tissue demonstrated that the Δ*tuf*-infected group had significantly lower recruitment of immune cells and expression of inflammatory markers than the WT-infected and pDL278*tuf*Δ*tuf*-infected groups (Supplementary Fig. 1j–o). Taken together, these results suggest that EF-Tu of *Streptococci* plays a critical role in the development of periodontitis. The knockout of the *tuf* gene effectively inhibits bone resorption, reduces osteoclast levels, and diminishes inflammation, suggesting the potential of EF-Tu as a target for therapeutic interventions in periodontitis.

Secreted EF-Tu promotes cell-surface adhesion

The results from immunotransmission electron microscopy showed that while EF-Tu is primarily present in the cytoplasm of cells (94.8%) in the planktonic state, it predominantly localizes on the surface of cells (96.7%) within the adhesion bacteria (as shown in Fig. 2a–c). This result indicated that EF-Tu is secreted out to the cell surface and plays a role in cell-surface adhesion to promote biofilm formation, beyond its regular function in translation in the cytoplasm. To test this hypothesis, we first assessed its ability to attach to a stiff surface. We labeled purified EF-Tu with Fluorescein Isothiocyanate (EF-Tu-FITC) and incubated it on a coverslip. Using total internal reflection microscopy (TIRFM), we tracked the movement trajectory of EF-Tu-FITC and compared it to that of BSA (Supplementary Fig. 2a, b). Our analysis indicated that EF-Tu moved a shorter distance in a unit time than BSA, and the mean square displacement (MSD) α value of EF-Tu (0.02438) was significantly lower than that of BSA (0.04326) (Fig. 2d). Additionally, the frequency of displacement distribution showed that EF-Tu had a better protein adhesion effect than BSA (Supplementary Fig. 2c). These results suggest that EF-Tu located on the cell surface is capable of directly adhering to abiotic surfaces.

To simulate the cell-surface adhesion function of the cell-surface protein EF-Tu, we incubated EF-Tu-FITC with WT *S. oralis* on a coverslip (Supplementary Fig. 2d). We tracked the path bacterial cells moved on the surface and analyzed them with a $G(\Delta x, t)$ probability distribution curve, which represents the probability of the bacterial cell moving a certain distance (Δx) in a given unit time (t). Our analysis revealed that cells incubated with EF-Tu-FITC moved a shorter distance in the unit time than those unincubated or incubated with BSA-FITC cells (Supplementary Fig. 2e). The MSD analysis showed that the α value for *S. oralis* with EF-Tu-FITC was the lowest (0.3154) among the three groups (Fig. 2e). Additionally, the frequency distribution of the movement distances showed that bacteria incubated with EF-Tu-FITC exhibited a high frequency of short displacement distribution (Supplementary Fig. 2f). These results suggest that extracellular EF-Tu has a cell-surface adhesion effect.
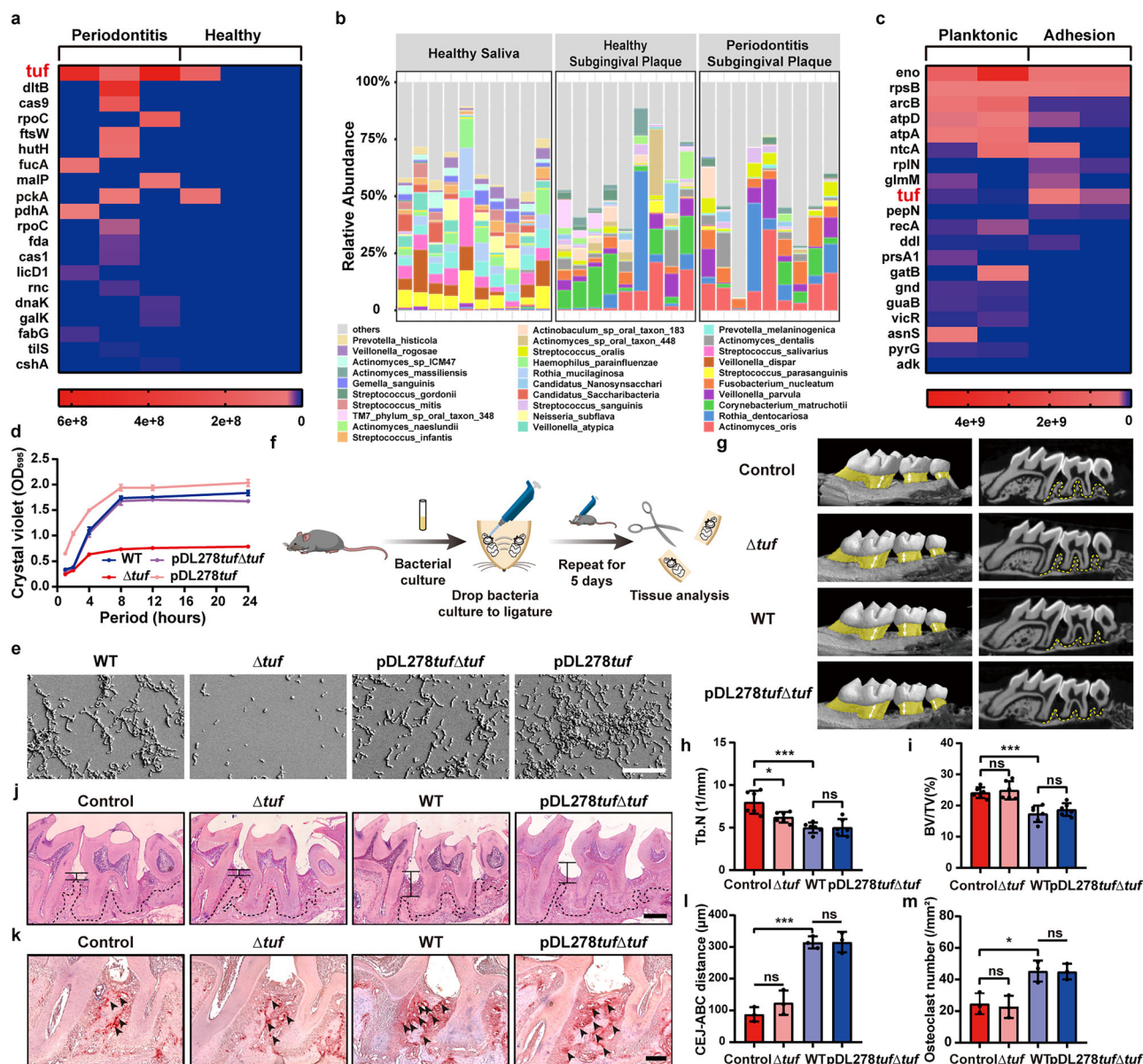
Fig. 1 | *Streptococci* EF-Tu is secreted to the bacterial surface and promotes biofilm development and periodontitis onset. a The heat map shows the relative abundance of the corresponding gene expression of *Streptococci* in subgingival plaque of periodontitis and healthy individuals. **b** Relative abundance analysis of species in different sample groups. The figure shows the top 30 contributing groups in the samples. **c** The heat map shows the relative abundance of the corresponding gene expression of *S. oralis* in biofilm and planktonic states. **d** Quantification of crystal violet staining of the biofilm during 24 h (*n* = 3). **e** SEM characterization of 1 h biofilms (scale bar, 20 μm.) **f** Schematic diagram of the experimental procedure of periodontitis mouse models. **g** The alveolar bone resorption measured by Micro-CT is represented as 3D viewing and a *Z*–*Y*-axis plane. The white arrow points to the CEJ-ABC distances, and the yellow area indicates the alveolar bone. **h, i** Quantitative analysis of the Tb. N and BV/TV of alveolar bone measured by Micro-CT (*n* = 6). **j** HE staining to characterize the alveolar bone height (scale bar, 300 μm.) **k** TRAP staining to characterize the extent of osteoclast infiltration in the alveolar bone (scale bar, 150 μm). **l** Quantitative analysis of CEJ-ABC distances (*n* = 3). **m** Quantitative analysis of the number of osteoclasts per unit area (*n* = 3). *Data information*: In **h, i, l, m** bars and error bars represent mean ± SD. Data were analyzed using One-way ANOVA. ns means no significance, *P < 0.05, **P < 0.01, ***P < 0.001.

Consistently, Δ*tuf* strain showed higher *G* (Δ*x*, *t*) probabilities over larger distances (Δ*x*) than those of the WT strain, suggesting that the deletion of EF-Tu reduces cell-surface adhesion. This was further supported by the fact that the rescued strain pDL278*tuf*Δ*tuf* reversed the *G* (Δ*x*, *t*) probabilities to the levels of WT strain (Fig. 2f). The MSD analysis showed that α value for Δ*tuf* (16.48) was the greatest among the four strains, whereas the rescued strain pDL278*tuf*Δ*tuf* (3.188) could recover or even reduce the α value to levels comparable to the WT (4.620). On the other hand, the overexpressed strain pDL278*tuf* (2.052) showed the smallest α value (Fig. 2g). Furthermore, the displacement frequency of Δ*tuf* was larger in the short movements than that of WT (Supplementary Fig. 2g). These results suggest

that EF-Tu plays a key role in bacterial surface adhesion and influence the early stages of biofilm formation.

"Barrel-like adhesion domain" of EF-Tu is responsible for cell-surface adhesion effects

To understand the mechanism underlying EF-Tu-mediated cell-surface adhesion, we first analyzed EF-Tu protein structure and revealed that the ED3 domain potentially plays a role in cell-surface adhesion (Supplementary Fig. 2h). Molecular dynamics simulations showed that within the ED3 domain, nine amino acids (R208, R227, R234, R241, R267, K268, R284, R288, R293) have significant adsorption potential to both the surface of
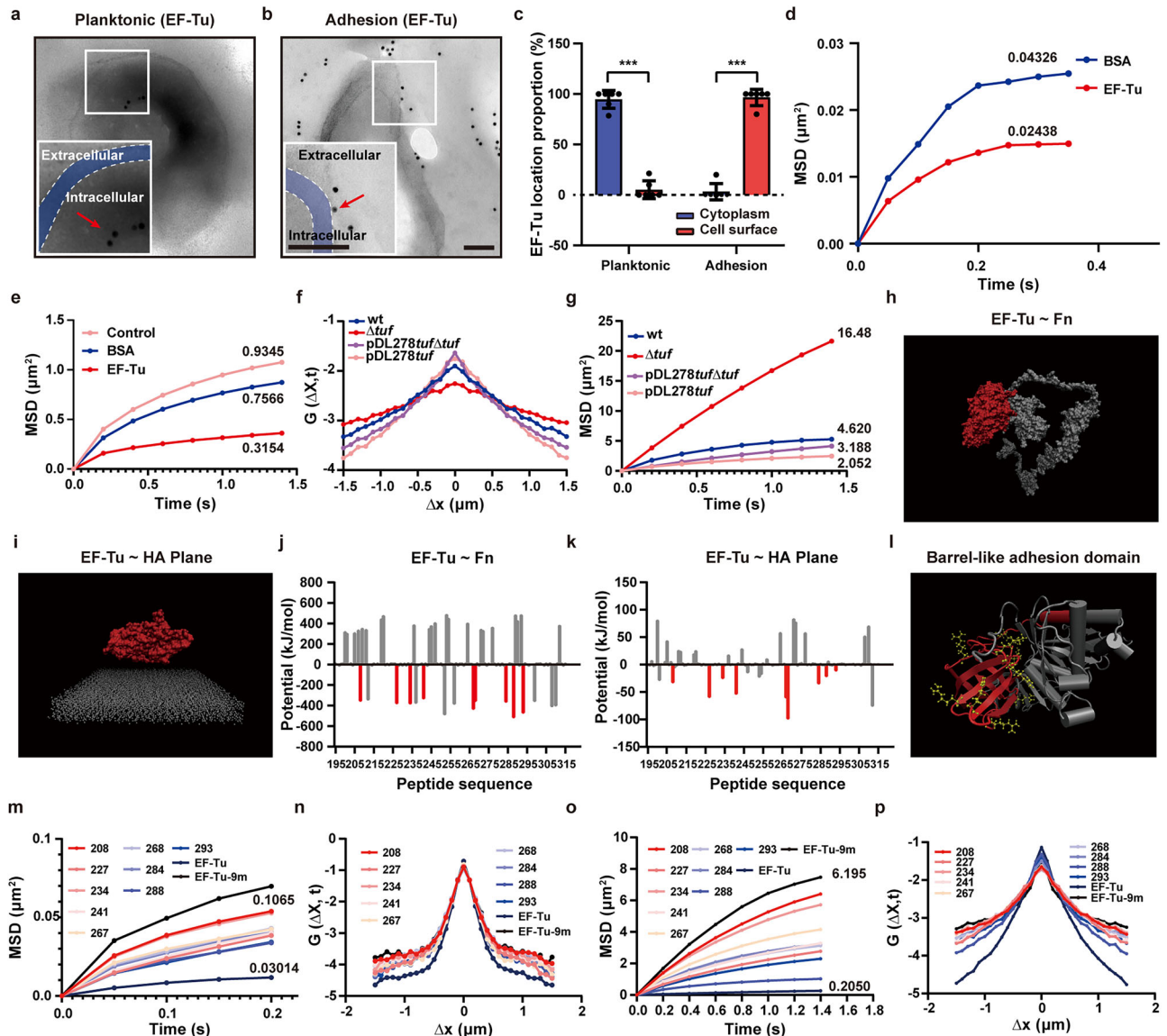
Fig. 2 | EF-Tu is the adhesion protein functioning with the "Barrel-like adhesion domain". a, b Immunotransmission electron microscopy images to characterize the cellular localization of EF-Tu in the planktonic and biofilm states of *S. oralis*. The purple area enclosed by the white dashed box indicates the bacterial membrane. The red arrow points to EF-Tu (scale bar, 100 nm). **c** Quantification analysis of EF-Tu location in images (*n* = 6). **d** The MSD versus time interval of BSA and EF-Tu. α value is shown along the curve. **e** The MSD versus time interval of three groups of *S. oralis*. α value is shown along the curve. **f** The step-size distribution of *S. oralis* at Δ*t* = 0.22 s. **g** The MSD versus time interval of *S. oralis*. **h** Molecular dynamics simulation of EF-Tu binding to Fn. Red represents EF-Tu, and silver represents Fn. **i** Molecular dynamics simulation of EF-Tu adhering to the HA plane. Red represents

EF-Tu, and silver represents the HA plane. **j, k** The potential energy of amino acid residues in the ED3 domain. The red bar represents the adhesive amino acid residues in both simulated systems. **l** The "Barrel-like adhesion domain" consists of the adhesive amino acid residues in both simulated systems. The silver represents EF-Tu, the yellow represents the "Barrel-like adhesion domain", and the red represents the ED3 domain. **m** The MSD versus time interval of eleven groups of EF-Tu proteins. **n** Step-size distribution of EF-Tu in protein groups at Δ*t* = 50 ms. **o** The MSD versus time interval of eleven groups of *S. oralis*. **p** Step-size distribution of EF-Tu in *S. oralis* groups at Δ*t* = 0.22 s. *Data information*: In **c**, bars and error bars represent mean ± SD. Data were analyzed using Two-way ANOVA. ns means no significance, *$P < 0.05$, **$P < 0.01$, ***$P < 0.001$.

fibronectin (Fn), a multifunctional adhesive glycoprotein in extracellular matrix and hydroxyapatite (HA), the material constituting dental surface (Fig. 2h–k and Supplementary Fig. 2i–l). Out of these nine amino acids, seven (R208, R227, R234R, K268, R284, R288, R293) are conserved among different bacteria (Supplementary Fig. 2h). Given that these nine amino acids are distributed across a barrel-like structure domain within EF-Tu, we have named it as "Barrel-like adhesion domain" (Fig. 2l).

Through mutagenesis and trajectory tracking, the adhesion effects of the "Barrel-like adhesion domain" were experimentally evaluated. We generated nine mutants, each with a single amino acid mutation (R208A, R227A, R234A, R241A, R267A, K268A, R284A, R288A, R293A), and a

mutant with all nine amino acids mutated (EF-Tu-9m). The results showed that both the MSD α value and the *G* (Δ*x*, *t*) probabilities of all the mutated proteins were significantly higher than those of the WT EF-Tu protein. Among the mutants, EF-Tu-9m exhibited the highest values (Fig. 2m, n). These results indicate that mutation of the "Barrel-like adhesion domain" reduced the surface adhesion effects of the EF-Tu protein. The frequency distribution of displacement results confirmed these observations (Supplementary Fig. 2n). Furthermore, the trajectory tracking results of the bacteria were in line with the protein adhesion findings (Fig. 2o, p and Supplementary Fig. 2o). Collectively, these findings suggest that the "Barrel-like adhesion domain" plays a crucial role in adhesion function of EF-Tu.
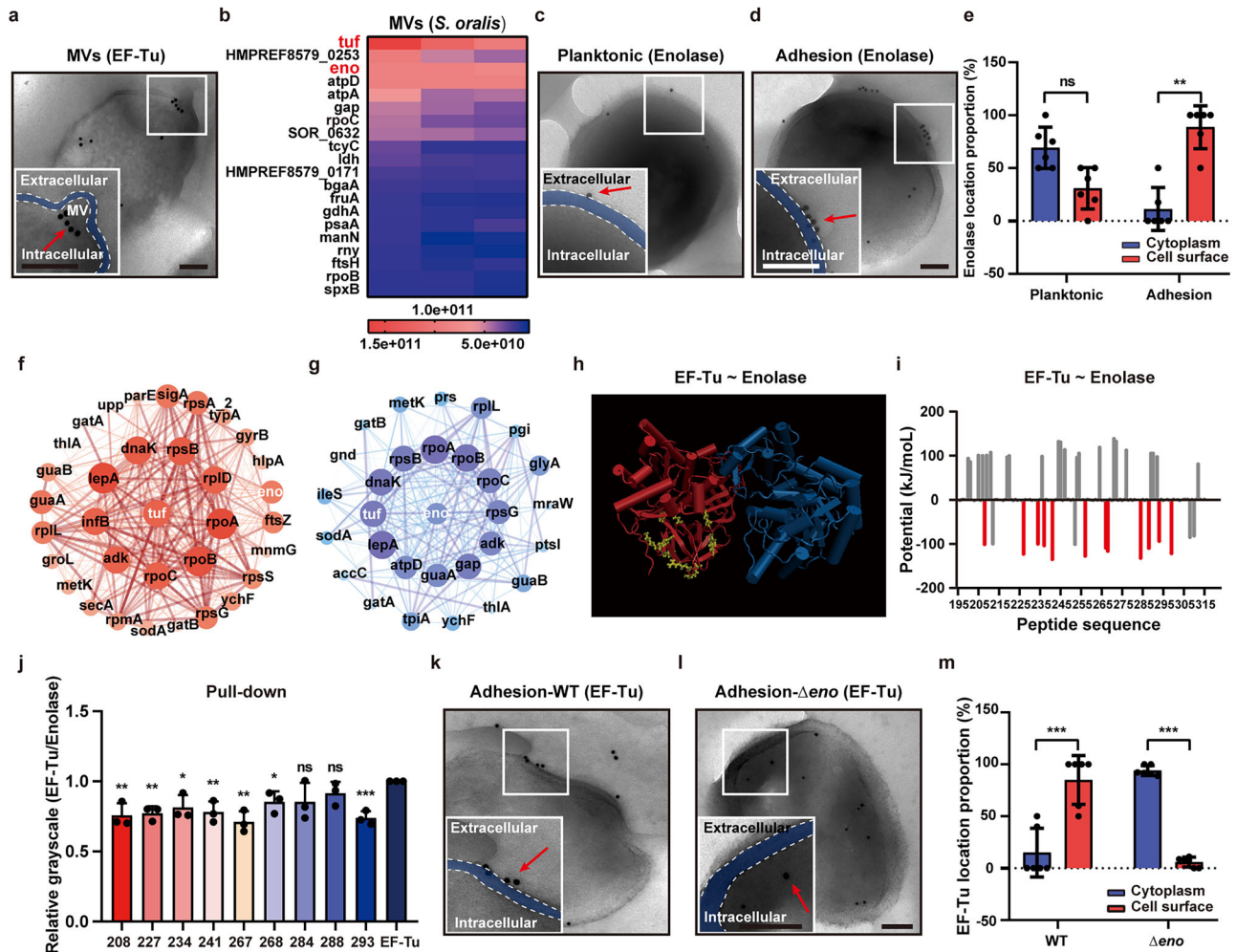
Fig. 3 | EF-Tu is secreted to the bacterial surface via membrane vesicles interacting with Enolase. a Immunoelectron electron microscopy photographs to characterize MV secretion in biofilm *S. oralis*. The purple area enclosed by the white dashed box represents the bacterial membrane undergoing secretion. The red arrow points to EF-Tu (scale bar, 100 nm). **b** Heat map of protein contents in MVs measured by MS. **c, d** Immunotransmission electron microscopy images to characterize the cellular localization of Enolase in the planktonic and biofilm states of *S. oralis*. The purple portion enclosed by the white dashed box indicates the bacterial membrane and the red arrow points to Enolase (scale bar, 100 nm). **e** Quantification analysis of Enolase location in images (*n* = 6). **f, g** The protein interaction network analysis to characterize the interaction proteins of EF-Tu and Enolase in *S. oralis* by pull-down assay. **h** The simulation systems of EF-Tu and Enolase. Red represents

EF-Tu, yellow represents the "Barrel-like adhesion domains", and blue represents Enolase. **i** Amino acid residue potentials of the ED3 domain. The red bar represents the residue potential energy of the "Barrel-like adhesion domain". **j** Western blot quantification of grayscale values. **k, l** Immunotransmission electron microscopy photography to characterize the cellular localization of EF-Tu in the *S. oralis* of WT and Δ*eno* strains. The purple portion enclosed by the white dashed box indicates the bacterial membrane, and the red arrow points to EF-Tu (scale bar, 100 nm). **m** Quantification analysis of EF-Tu location in images (*n* = 6). *Data information*: In **e, j, m**, bars and error bars represent mean ± SD. Data were analyzed using two-way ANOVA (**e, m**) and unpaired *t*-test (**j**). ns means no significance, *$P < 0.05$, **$P < 0.01$, ***$P < 0.001$.

EF-Tu is secreted to the cell surface through membrane vesicles

Immunotransmission electron microscopy showed that EF-Tu secreted into the bacterial cell surface of adherent *S. oralis* via membrane vesicles (MVs) (Fig. 3a). We explored a static biofilm system to investigate if MV containing EF-Tu plays a role in cell-surface adhesion in early biofilm development. In this system, initial bacteria adherence to the surface is measured by microcolony formation on the surface. We first extracted MVs from EF-Tu knockout strain and WT strains (Supplementary Fig. 3a) and incubated them with *S. oralis* cultures at gradient concentrations. Quantitative crystal violet staining showed that MVs of the WT strain enhance microcolony formation in a dose-dependent manner, while MVs from the Δ*tuf* strain showed little enhancing effect even with a very high concentration (Supplementary Fig. 3b, c). These results suggest that EF-Tu facilitates cell-surface adhesion through the secretion via MVs.

We then purified MVs from the WT strain for MS analysis to identify the MV proteome. The results revealed that in addition to a high level of

EF-Tu in MVs, Enolase, a known secretory protein of the MV pathway[35,36], also has a high level in MVs (Fig. 3b). Immunotransmission electron microscopy showed that both EF-Tu and Enolase enriched on bacterial cell surfaces in biofilm culture in contrast to planktonic culture (Fig. 3c–e). Based on these observations, we hypothesized that EF-Tu interacts with Enolase and, thereafter, secrets through MVs. To prove this hypothesis, we expressed His6-tagged EF-Tu or Enolase in the WT strain and separated cytoplasm for pull-down assays. MS analysis showed that both EF-Tu and Enolase can pull down each other, indicating Enolase and EF-Tu could interact with each other in the cytoplasm (Fig. 3f, g). Subsequently, MicroScale Thermophoresis (MST) experiments were performed on rhodamine-labeled Enolase and purified EF-Tu protein, and bovine serum albumin (BSA) acted as a control. The dissociation constant of Enolase with EF-Tu ($K_d = 7.75\mathrm{e}{-11}$) was smaller than that of the control ($K_d = 2.71\mathrm{e}{-7}$), indicating that EF-Tu has a direct binding effect with Enolase (Supplementary Fig. 3d).

To confirm the direct interaction between Enolase and EF-Tu, both theoretical calculations and experimental validations were carried out. Firstly, a molecular dynamics simulation of the binding between EF-Tu and Enolase was conducted for 10 ns until reaching equilibrium states (Supplementary Fig. 3e–g). Analysis of the amino acid residue potential in the "Barrel-like adhesion domain" indicated that among the 10 docking models, EF-Tu had binding effects with Enolase (Fig. 3h, i). Subsequently, the pull-down experiments were performed on mutants of EF-Tu and purified Enolase protein, and the adhesion effects were quantified using Western blotting (Supplementary Fig. 3h, i). The results of these experiments confirmed that there is a direct interaction between EF-Tu and Enolase and that the "Barrel-like adhesion domain" serves as the binding domain for this interaction (Fig. 3j and Supplementary Fig. 3j).

To investigate the role of Enolase in the secretion of EF-Tu, we examined the localization of EF-Tu in the Enolase knockout mutant (Δeno). Immunotransmission electron microscopy revealed that while EF-Tu in wild-type (WT) strains could be secreted extracellularly, it only presents in the intracellular region in Δeno (Fig. 3k–m), indicating that the secretion of EF-Tu through MVs is Enolase-dependent.

Simeprevir inhibits cell-surface adhesion effects of EF-Tu

From the FDA drug library, the virtual drug screen identified simeprevir as a potential candidate to disrupt the cell-surface adhesion effect of EF-Tu, which could bind to the "Barrel-like adhesion domain" (Fig. 4a). Molecular dynamics simulations of the EF-Tu and simeprevir system and calculations of the potential energy of amino acid residues (Supplementary Fig. 4a) revealed that simeprevir potentially binds to the "Barrel-like adhesion domain" and inhibits the adhesion effects of EF-Tu (Fig. 4b). To assess its efficacy, a range of concentrations of simeprevir were added to cultures of *S. oralis* to measure its impact on bacterial adhesion. Results showed that the minimum inhibitory concentration (MIC) of simeprevir for *S. oralis* is 5 μM (Supplementary Fig. 4b), and a much lower concentration (1 μM) of simeprevir could effectively prevent *S. oralis* adhesion without interfering with cell growth (Supplementary Fig. 4c). We also measured the biofilm growth curves with or without simeprevir incubation by quantitative crystal violet staining. The results showed that simeprevir treatment significantly reduced the extent of biofilm formation over time in a dose-dependent manner (Fig. 4c).

To further determine whether simeprevir disrupts the cell-surface adhesion effects of EF-Tu, we performed trajectory tracking of bacteria with or without the presence of simeprevir. Our findings revealed that 1 μM simeprevir added in solution was able to significantly reduce bacterial cells' adhesion to the surface and enhance their motility (Supplementary Fig. 4d–f). To further confirm the drug's effect on the protein, we added different concentrations of simeprevir to the purified EF-Tu protein solution and tracked its motility using TIRFM. The results were consistent with the bacterial inhibition effect, indicating that simeprevir could inhibit the protein adhesion effect (Fig. 4d, e and Supplementary Fig. 4g). In addition, we also explored the impact of simeprevir on the secretory pathway. Western blotting was performed for the pull-down system of EF-Tu mutant proteins and Enolase with simeprevir (Supplementary Fig. 4h), and the quantitative results indicated that simeprevir could significantly inhibit the direct interaction of EF-Tu with Enolase (Fig. 4f). More specifically, simeprevir inhibited the binding of wild-type EF-Tu and mutants at residues 227, 234, and 268, indicating these are not critical binding sites. In contrast, residues 208, 241, 267, 284, 288, and 293 were identified as key drug-binding sites. These findings suggest that simeprevir can prevent the adhesion and secretion of EF-Tu by binding to the "Barrel-like adhesion domain".

Simeprevir provides prevention and supplementary treatment of periodontitis

To evaluate the effectiveness of simeprevir in the prevention of periodontitis, we daily dropped *S. oralis* with or without simeprevir to the ligature of the maxillary second molar of mice for 7 consecutive days. 1 μM simeprevir solution was used for the experiments as its inhibitory effect on adhesion and its lesser effects on bacterial growth were helpful for avoiding dysbiosis.

Subsequently, we analyzed the mice using Micro-CT (Fig. 4g). Our results showed that the group treated with a combination of *S. oralis* and simeprevir exhibited a significant inhibition in the reduction of BV/TV and Tb. N, in comparison to the group subjected only to *S. oralis* ligation (Fig. 4h–j). We further performed histological quantification to determine the extent of alveolar bone destruction, and the results obtained from HE staining revealed a significant inhibition of alveolar bone loss in the groups treated with simeprevir (Fig. 4k, l). Furthermore, these groups exhibited reduced osteoclast infiltration (Supplementary Fig. 4i, j). Overall, our study demonstrates that simeprevir effectively prevents periodontitis progression in animals.

To evaluate the potential of simeprevir for the prevention and treatment of clinical periodontitis, we established a periodontitis mouse model by transplanting subgingival plaque from periodontitis patients into mice over a period of 7 consecutive days (Supplementary Fig. 5a). Subsequent Micro-CT analysis showed that the addition with simeprevir in transplantation resulted in significant inhibition of reduction in BV/TV and Tb. N, compared to the group transplanted plaque alone (Fig. 5a–c). Consistent results were observed through HE staining and TRAP staining, which showed that the addition of simeprevir in transplantation effectively inhibited the resorption of alveolar bone (as indicated by CEJ–ABC distance) and the infiltration of osteoclasts, compared to the group transplanted plaque alone (Fig. 5d–g). These findings underscore the potential of simeprevir in preventing the development of periodontitis. Moreover, the addition of simeprevir in transplantation after the removal of ligatures showed a higher regeneration in BV/TV and Tb. N, compared to the group transplanted plaque alone, which assisted the efficacy of periodontal treatment (Fig. 5h–j). HE staining and TRAP staining confirmed the supplementary treatment efficacy of alveolar bone resorption and osteoclast infiltration in periodontitis mice treated with simeprevir (Supplementary Fig. 5b–e). These results suggest that simeprevir exhibits a potential treatment effect for periodontitis.

Mouthwash with simeprevir inhibits human dental plaque formation

We recruited six volunteers to investigate the potential effects of simeprevir in preventing plaque formation in the human oral cavity. In the control trial, the volunteers underwent oral hygiene cleaning to remove plaque from the tooth surface. Subsequently, they rinsed their mouths with double-distilled water for 30 s without brushing. Plaque staining was performed at various time intervals (0, 1, 2, 4, 6, and 8 h post-rinse) for photography. Following the control trial, we conducted an experimental trial with the same group of volunteers. Once again, they underwent oral hygiene cleaning and then rinsed their mouths with 1 μM simeprevir mouthwash for 30 s without brushing. Plaque staining was performed at the same time intervals (0, 1, 2, 4, 6, and 8 h post-rinse) for photography (Fig. 6a). The results showed that rinsing with simeprevir mouthwash led to lower values of Quigley–Hein plaque index (Fig. 6b–d), suggesting that simeprevir is effective in inhibiting the formation of human dental plaque. Additionally, subgingival plaque samples were collected from the volunteers at 24 and 48 h post-rinse with water or simeprevir, and these samples were cultured for colony counting assays. The results showed a significantly lower number of colonies formed after simeprevir rinse (Fig. 6e), providing further confirmation of the inhibitory effect of simeprevir on plaque formation in the human oral cavity.

Building on the inhibitory effect of simeprevir on human oral plaque formation, we extended its application to daily oral hygiene measures as an aid in both periodontitis prevention and supplementary treatments. In a similar fashion, volunteers underwent oral hygiene cleaning to remove plaque from their dental surfaces. Subsequently, they rinsed their mouths with simeprevir mouthwash for 30 s after tooth brushing, twice a day. Plaque staining was conducted at various time intervals (0, 1, 3, 5, and 7 days) for photography. In the control trial, double-distilled water was used instead of simeprevir (Fig. 6f). The results demonstrated that the application of simeprevir resulted in improved oral hygiene, exhibiting a reduction in the Quigley–Hein plaque index compared to the water control (Fig. 6g–i).
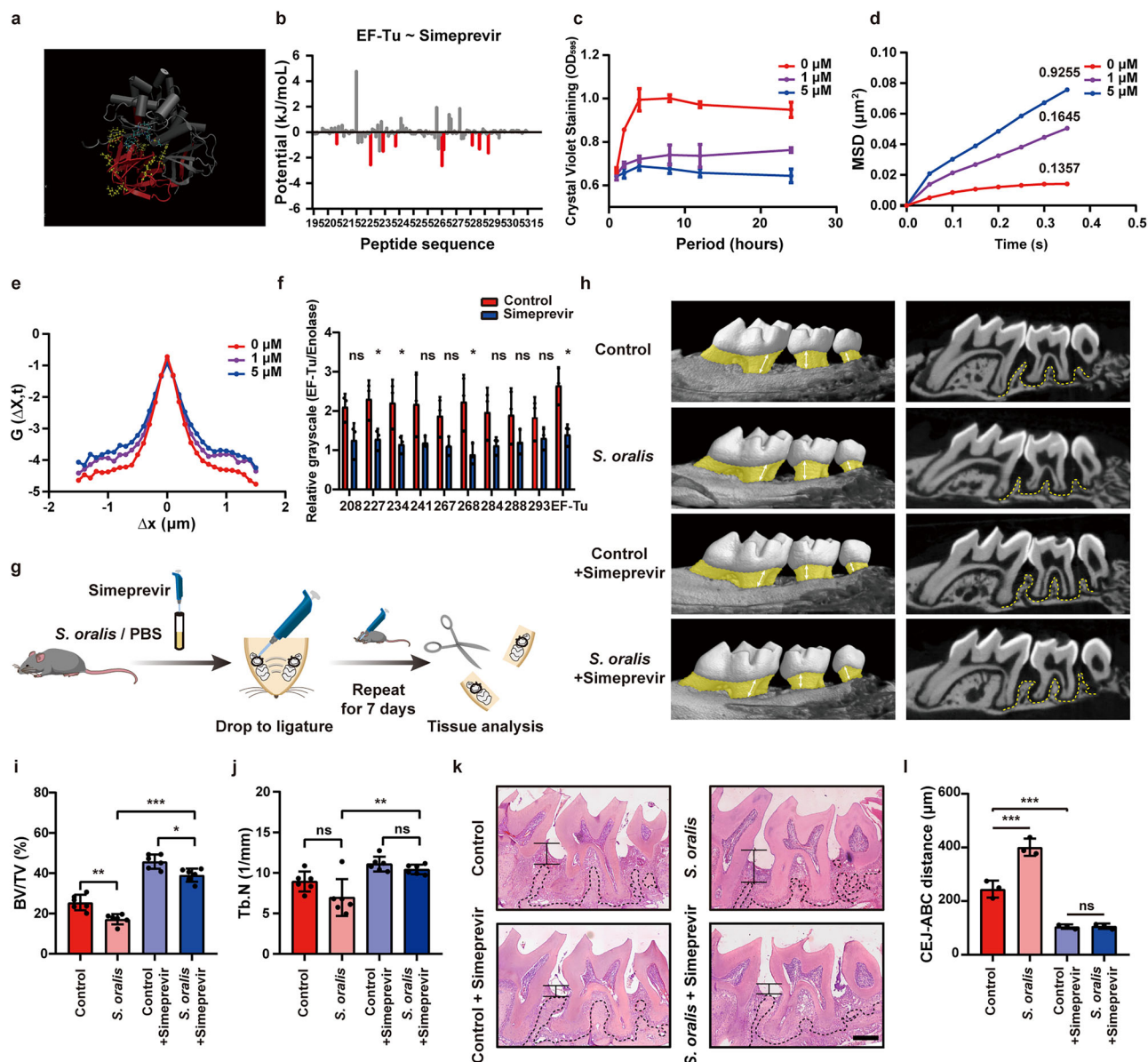
Fig. 4 | Simeprevir inhibits EF-Tu function to prevent the onset of periodontitis. **a** Molecular dynamics simulation of simeprevir binding to EF-Tu. Blue represents simeprevir, red represents the ED3 domain, yellow represents the "Barrel-like adhesion domain", and silver indicates EF-Tu. **b** Amino acid residue potentials of the ED3 domain. The red bar represents the residue potential energy of the "Barrel-like adhesion domain". **c** Quantification of crystal violet staining to measure the biofilm growth curve of *S. oralis* ($n = 6$). **d** The MSD versus time interval of three groups of proteins. α value is shown along the curve. **e** Step-size distribution of EF-Tu protein groups at $\Delta t = 50$ ms. **f** Western blot quantification of relative gray values. Unpaired *t*-test ($n = 3$). **g** Schematic diagram of the experimental procedure of periodontitis mouse models. **h** The alveolar bone resorption measured by Micro-CT is represented as 3D views and a *Z*–*Y* axis plane. The white arrow points to the CEJ–ABC distances, and the yellow area indicates the alveolar bone. **i, j** Quantitative analysis of BV/TV and Tb. *N* measured by micro-CT. One-way ANOVA ($n = 6$). **k** HE staining to characterize the alveolar bone height (scale bar, 300 μm). **l** Quantification analysis of CEJ–ABC distances. One-way ANOVA ($n = 3$). *Data information*: In **h, i, l, m** bars and error bars represent mean ± SD. ns means no significance, *$P < 0.05$, **$P < 0.01$, ***$P < 0.001$.

Collectively, these findings demonstrate the effectiveness of simeprevir in inhibiting oral plaque formation and suggest a potential therapeutic strategy for the prevention and treatment of periodontitis.

Discussion

The primary cause of periodontitis is attributed to the formation of dental plaque biofilm, which is a diverse microbial community present in the oral cavity[37]. Although current therapies provide temporary plaque removal and mitigate disease progression, the persistent recurrence of periodontitis is frequently linked to the cyclical reformation of oral biofilm. The pivotal role of dental plaque biofilm in the clinical challenges posed by periodontitis underscores the critical necessity to delve into the underlying etiological

mechanisms governing biofilm formation. This exploration holds the key to fundamental advancements in the treatment and prevention of periodontitis.

To initiate subgingival plaque biofilm formation, *Streptococci*, such as *S. oralis* first adhere to the dental surface, followed by interacting with other flora to form a mature and pathogenic biofilm. *P. gingivalis* is a major pathogenic bacterium that not only plays a critical role in the progression of periodontitis but is also strongly associated with systemic diseases, including Alzheimer's disease. Periodontitis has been shown to have a significant connection with Alzheimer's disease. Emerging evidence suggests that the inflammatory and microbial mechanisms involved in periodontitis may contribute to the onset and progression of Alzheimer's disease[6,7,38].
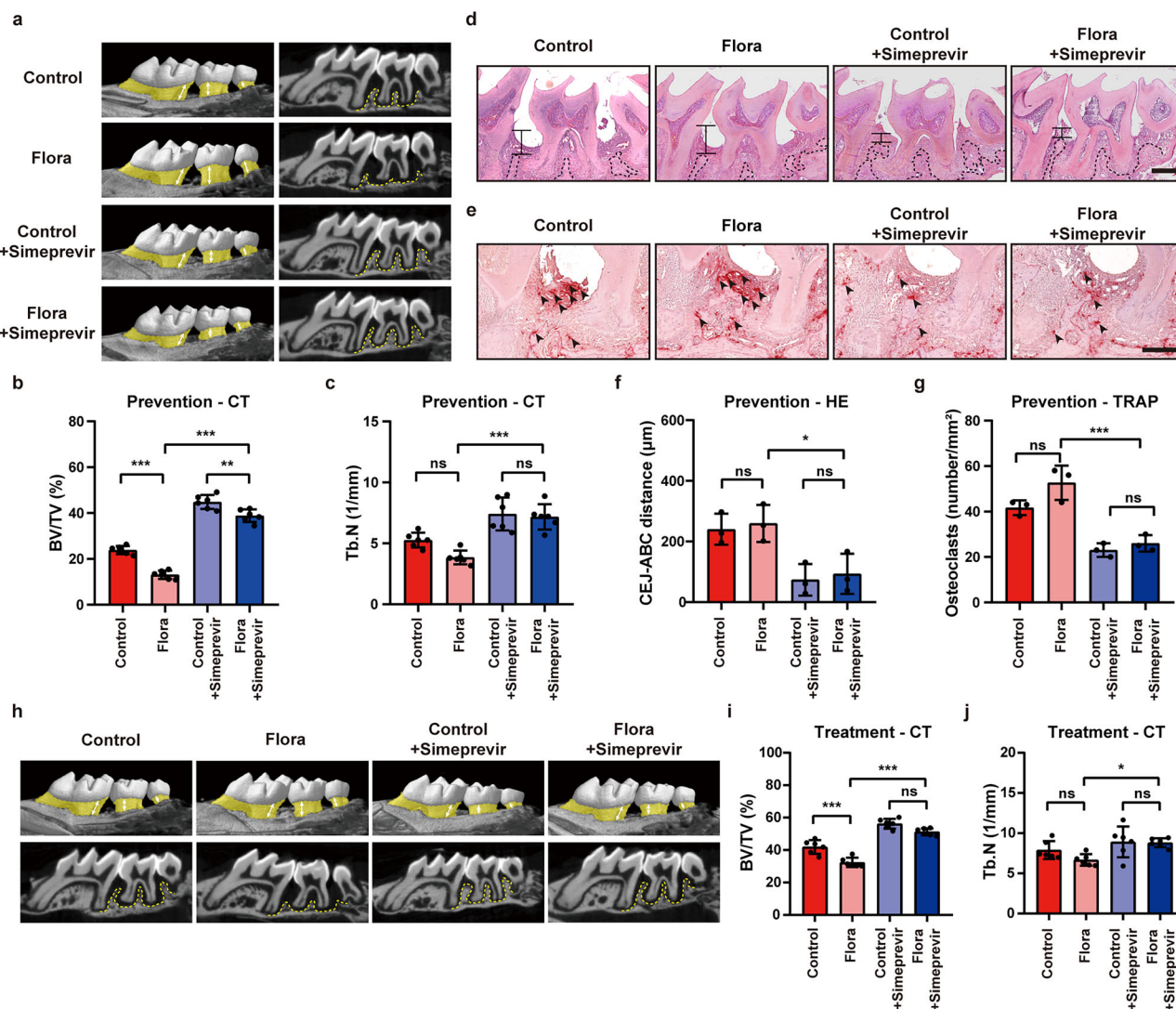
Fig. 5 | Simeprevir provides prevention and supplementary treatment for plaque-transplanted periodontitis mouse models. a, h The alveolar bone resorption measured by Micro-CT is represented as 3D views and a Z–Y-axis plane. The white arrow points to the CEJ–ABC distance and the yellow area indicates the alveolar bone. **b, c, i, j** Quantitative analysis of BV/TV and Tb. *N* measured by Micro-CT. One-way ANOVA (*n* = 6). **d** HE staining to characterize the alveolar bone height (scale bar, 300 μm) **e** TRAP staining to characterize the extent of osteoclast infiltration in the alveolar bone (scale bar, 150 μm). **f** Quantification analysis of CEJ-ABC distance. One-way ANOVA (*n* = 3). **g** Quantification analysis of the number of osteoclasts per unit area. One-way ANOVA (*n* = 3). ns means no significance, *$P < 0.05$, **$P < 0.01$, ***$P < 0.001$.

P. gingivalis attaches to *Streptococci* by adhering to glyceraldehyde-3-phosphate dehydrogenase (GAPDH) on the surface of the *Streptococci* with its primary fimbriae (FimA) and to the streptococcal cell surface proteins SspA/B with its minor fimbriae (Mfa) to form biofilms[20,39,40]. *F. nucleatum* acts as an intermediary between early and late colonizers, forming "corn-cob" structures with *Streptococci*. This enhances biofilm stability and pathogenicity[41]. *Aggregatibacter actinomycetemcomitans* (*A. actinomycetemcomitans*) is a significant pathogen in locally invasive periodontitis. *S. gordonii* secretes lactic acid as a carbon source for *A. actinomycetemcomitans* and the biofilm is more pathogenic when the two are symbiotic[42–44]. Therefore, streptococcal biofilms not only mediate the physical adhesion of late colonizers but also interact with other oral microorganisms to modulate the structure and function of subgingival plaque, playing a crucial role in subgingival plaque formation and pathogenesis.

The mechanism by which *Streptococci* adhere to the dental surface remains unknown, as these Gram-positive bacteria lack flagella and cannot use mechanosensory signals to reach the surface like Gram-negative bacteria. Current studies have focused on the role of streptococcal adhesins.

However, it is important to note that the effects of adhesins are species-specific and not generalized or conserved across all *Streptococci*. Therefore, our research aimed to identify the bacterial surface proteins responsible for *Streptococcal* adhesion to dental surfaces.

Our study discovered that EF-Tu is highly expressed on the surface of *Streptococci* in subgingival plaque of periodontitis and has a conserved structure across different bacterial genera. It is mainly an elongation factor in protein synthesis in the cytoplasm, but recent studies suggest that its secretion to the bacterial surface may play a role as a moonlighting protein. EF-Tu is a protein that binds to CD21 in B lymphoma cells and activates the host immune system[45]. In addition to activating the immune system, EF-Tu from *S. aureus* and *Staphylococcus epidermidis* (*S. epidermidis*) binds to neuropeptide hormone substance P (SP) and stimulates inflammatory responses[46–48]. EF-Tu also facilitates bacterial adhesion and host cell invasion. M. pneumoniae EF-Tu binds to actin, fibrinogen, laminin, and fibrinogen[49]. However, the role of EF-Tu in periodontitis has not been reported yet, and its mechanisms of secretion and adhesion during biofilm formation are still unclear.
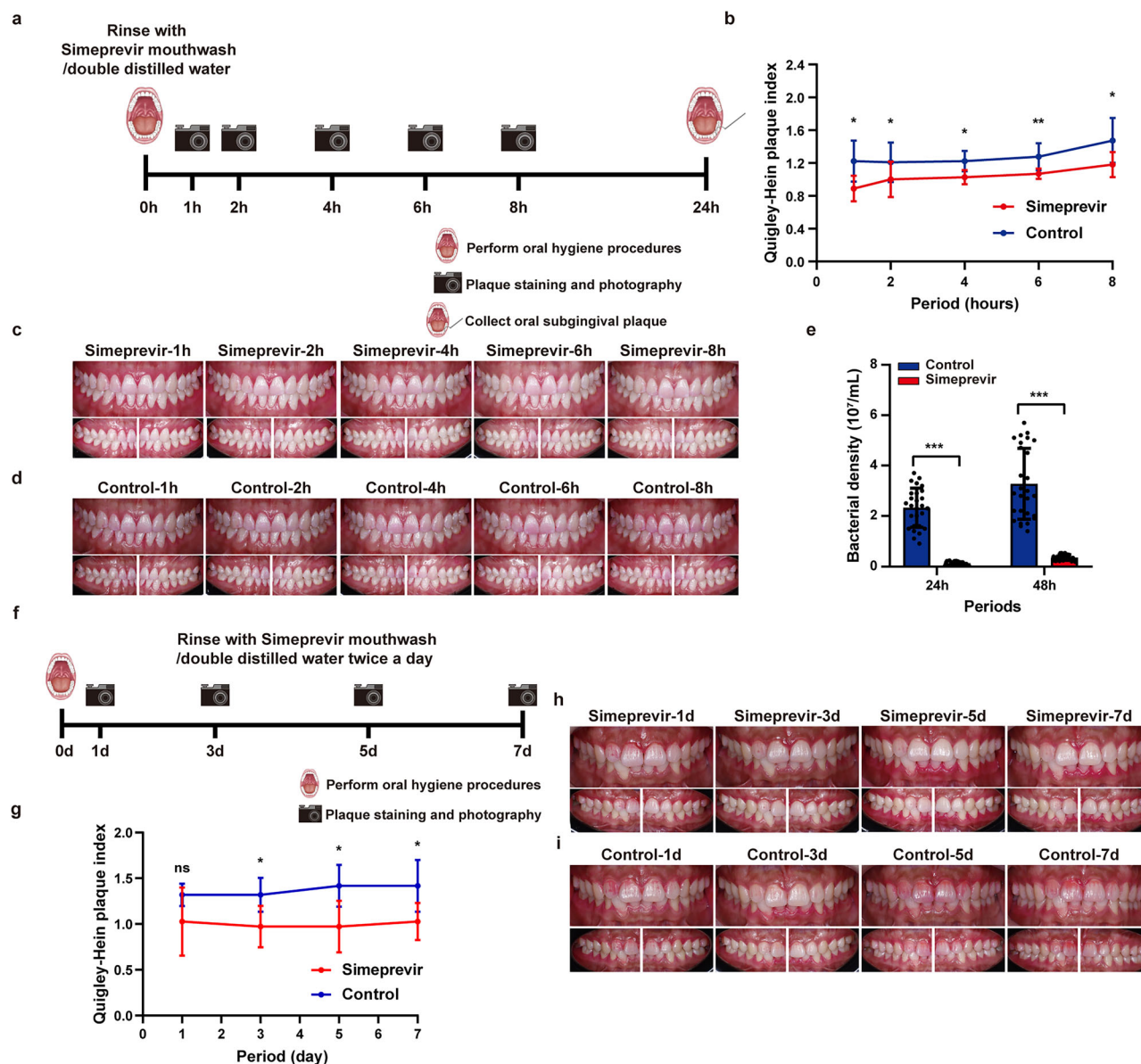
Fig. 6 | Simeprevir mouthwash inhibits the growth of oral plaque. a Schematic diagram of the experiment for dynamic observation of oral plaque growth without brushing teeth. **b** Curves of Quigley–Hein plaque index over time. Paired t-test ($n = 6$). **c, d** Front and side views of the oral cavity with plaque staining after using simeprevir mouthwash or double-distilled water. **e** Bacterial density of subgingival plaque in the oral cavity under different treatments. Two-way ANOVA ($n = 27$). **f** Schematic diagram of the experiment for dynamic observation of oral plaque growth with brushing teeth. **g** Curves of Quigley–Hein plaque index with periods. Paired t-test ($n = 6$). **h, i** Front and side views of the oral cavity with plaque staining by using simeprevir mouthwash or double-distilled water after brushing teeth. ns means no significance, *$P < 0.05$, **$P < 0.01$.

The study found that EF-Tu is secreted to the bacterial surface and plays a crucial role in surface adhesion. The interaction of EF-Tu with membrane protein Enolase facilitates the secretion of EF-Tu through membrane vesicles. By blocking this secretion pathway, we can effectively prevent biofilm formation and the progression of periodontitis. The cell-surface adhesion effect of secreted EF-Tu is mediated by its "Barrel-like adhesion domain".

Current treatments, such as scaling, scraping, and periodontal surgery, provide only temporary removal of subgingival plaque, but repeated subgingival plaque formation often leads to recurrent, difficult-to-cure periodontitis. Chlorhexidine is a commonly used antimicrobial agent for periodontal adjuvant therapy. However, it can cause mucosal irritation and oral flora dysbiosis, which can result in diseases[50]. Combining the clinical problems with the results of the present study, we performed a virtual drug screen in the FDA drug library based on the EF-Tu protein

structure, followed by experimental tests. We found that simeprevir, an FDA-approved drug, binds to the "Barrel-like adhesion domain" of EF-Tu, effectively inhibiting cell-surface attachment and biofilm formation. Simeprevir is an antiviral drug used to treat hepatitis C virus infections. However, there are no studies reporting its effectiveness in inhibiting streptococcal biofilm or treating periodontitis. The study showed that simeprevir provides prevention and supplementary treatments for periodontitis in humanized periodontitis mouse models, and effectively inhibits dental plaque formation in clinical trials. simeprevir demonstrated the ability to inhibit EF-Tu secretion and biofilm formation in preclinical studies, while clinical trials validated its efficacy in reducing plaque formation, measured by plaque index as a standard. Future studies will include metagenomic sequencing to further clarify simeprevir's mechanism of action and its effects on subgingival plaque composition, enhancing its potential as a clinical therapy for periodontitis. These

findings provide potential clinical strategies for preventing and supplementary treatment periodontitis.

Methods

Strains, constructs, and growth conditions

The strains used in the study are listed in Supplementary Table 1, the plasmids are listed in Supplementary Table 2, and the primers are listed in Supplementary Table 3. *S. oralis* was grown at 37 °C in the aerobic environment with Trypticase Soy Broth (TSB, Hope Bio-Technology) medium and TSB agar plates (TSB medium with 15 g/L agar). The knockout strains were constructed by replacing the target gene with the kanamycin gene sequences by homologous recombination. Fragments with ~500 bp each of the upstream and downstream of the target gene and the kanamycin gene sequences were introduced into *S. oralis* by competence stimulating peptide (CSP). The single clones were picked up on the TSB agar plates with kanamycin resistance for mutant identification. The overexpressed strains were constructed by introducing the plasmids inserted with the target gene into *S. oralis* by CSP and identified on the TSB agar plates with spectinomycin resistance. Complementary strains were constructed by introducing the overexpression plasmids into the mutant strains, which were picked up on the TSB agar plates with dual resistance to spectinomycin and kanamycin. *S. oralis* with overexpressed plasmids was induced with 8 mM inducer isopropyl-β-D-thiogalactoside (IPTG) at 37 °C for 1 h to complete the gene overexpression. If required, the following final concentrations of antibiotics were added to *S. oralis* culture medium: spectinomycin (1 mg/mL) and kanamycin (50 μg/mL).

E. coli DH5α was used for cloning and plasmid replication, and *E. coli* BL21 (DE3) was used for protein purification. *E. coli* was grown in the LB (Luria-Bertani, Sangon Biotech) broth medium and the LB agar plates (LB medium with 15 g/L agar) at 37 °C. The homologous recombinant plasmids were introduced into *E. coli* and single clones were picked up on the LB agar plates with resistance. If required, the following final concentrations of antibiotics were added to the *E. coli* culture medium: ampicillin (100 μg/mL) and kanamycin (50 μg/mL).

Protein purification

EF-Tu protein was produced and purified from freshly transformed *E. coli* BL21 (DE3) cells, which contained pET28a expression plasmids carrying the *tuf* gene[35,36,51,52]. The *tuf* gene was subcloned into the vector pET28a as a NdeI-HindIII fragment by homologous recombination and transformed into *E. coli* BL21 (DE3). *E. coli* BL21 (DE3) colonies were picked and resuspended in the LB medium containing kanamycin and incubated in a shaker at 37 °C until the absorbance (OD_{600}) reached 0.6–0.8. The expression of recombinant protein was induced with 0.5 mM IPTG at 18 °C. After 16 h, *E. coli* BL21 (DE3) cells were collected and stored at −80 °C. To purify the proteins, cell precipitates were resuspended in the buffer at pH 7.5 containing 20 mM Tris–HCl, 100 mM NaCl, 1 mM DNase I, 1 mM PMSF, and 2 mM $MgCl_2$. After being mixed well on ice, the cells were lysed by ultrasonication. The cell lysate was centrifuged at 4 °C, 12,000×*g* for 30 min, and the supernatant was incubated with Ni-NTA resin. The resin was washed sequentially with buffer A at pH 7.5 containing 20 mM Tris–HCl, 100 mM NaCl, 20 mM imidazole, and buffer B at pH 7.5 containing 20 mM Tris–HCl, 100 mM NaCl, and 100 mM imidazole. The final protein was eluted from the column with the elution buffer at pH 7.5 containing 20 mM Tris–HCl, 100 mM NaCl, and 300 mM imidazole. Protein concentration was measured using the BCA Protein Quantification Kit (Vazyme).

Metagenomic analysis

The information on the samples is listed in Supplementary Table 4. Quality assessment of raw sequencing data and quality control (QC) of sequencing data were achieved by FastQC. After QC, host DNA sequences were removed by KneadData and bowtie2[53]. Subsequently, the species in clean data were annotated and classified using MetaPhlAn, and count tables were generated by executing the "rel_ab_w_read_stats" command[54]. The HUMAnN was used to analyze the functional information of microorganisms to obtain information on genes, pathways, and members of associated microbial communities. Subsequently, the relative abundances of different species and count tables were imported into the R software for further diversity analysis, statistical tests, and visualization. R packages such as ggplot2[55], RcolorBrewer[56], ggsignif[57], ade4[58], and vegan[59] were used for downstream analysis. The biodiversity corresponding to the different groups was assessed by the values of α and β diversity. Principal co-ordinates analysis (PCoA) was implemented by using the ade4 package and mapped using the ggplot2 package. *P*-values corresponding to the relative abundances of different species in three groups were calculated by the Wilcoxon test using the ggsignif package.

For co-occurrence network analysis, correlations among species in each group were calculated based on the relative abundance at the species level. The thresholds for species' relative abundance were all set at relative abundance >1% and occurring in more than 20% of the samples and the correlations between species were calculated based on Spearman. The final correlation values of $|r| \geq 0.6$ and $p < 0.05$ were used for downstream analysis.

MS and pathway analysis

Overnight strains were diluted to absorbance OD_{600} was 0.1 for preparation. For bacterial surface protein sample collection, the treated *S. oralis* was collected by centrifugation and washed with a solution containing 40% sucrose (SCR) and 20 mM sodium azide (SCR). Immobilized trypsin (Thermo Fisher Scientific, Waltham, MA, USA), which had been activated with 50 mM ammonium bicarbonate (SCR), was added to the bacterial precipitate and reacted at 37 °C for 45 min. The isolated bacterial surface protein peptides were then collected and performed electrophoresis and Coomassie Brilliant Blue staining.

Clinical samples were obtained from healthy and periodontitis volunteers. Saliva samples were obtained by collecting 5 mL of saliva from volunteers, and subgingival plaque was obtained by scraping subgingival plaque from multiple tooth sites with a probe and collecting it in PBS. Samples were snap-frozen in liquid nitrogen immediately after collection and stored at −80 °C.

The corresponding gels were cut and decolorized with 50% acetonitrile (ACN)-50% 50 mmol/L NH_4HCO_3. Dithiothreitol (DTT), iodoacetamide (IAA), and 50% ACN–50% 50 mM NH_4HCO_3 were added sequentially to the decolorized samples to reduce alkylation. The samples were digested with trypsin, and the peptides were obtained with an extraction solution. The enzymatically cleaved peptides were desalted using a self-filling desalting column, and the solvent was evaporated in a vacuum centrifuge concentrator at 45 °C. Peptides were captured using Easy-nLC 1200 (ThermoFisher Scientific, USA) and 150 μm × 15 cm in-house-made column packed with Acclaim PepMap RPLC C18 (1.9 μm, 100 Å, Dr. Maisch GmbH, Germany). The samples were eluted from the capture column by mobile phase A: 0.1% formic acid in water and mobile phase B: 20% 0.1% formic acid in water–80% acetonitrile.

The nanoLC system was coupled to a Q Exactive™ Hybrid Quadrupole-Orbitrap™ Mass Spectrometer (Thermo Fisher Scientific, USA), which was operated at a Spray voltage of 2.2 kV and a Capillary temperature of 270 °C. The MS resolution was 70,000 at 400*m/z*, and the MS precursor *m/z* range was 300.0–1800.0. The top 20 most intense peptide ions from the preview scan in the Orbitrap were collected for the next step of MS analysis[60]. The MS raw files were analyzed using MaxQuant. The peptides identified with high confidence were selected for downstream protein identification analysis.

The protein abundance avidity was analyzed using GraphPad Prism 8.0. The KOBAS 3.0 web tool was used to perform the KEGG pathway analysis[61], and the STRING database was used to complete the GO enrichment analysis[62]. The results of the KEGG pathway and GO enrichment analyses were visualized by the ggplot2 package. The co-occurrence network was implemented based on the R package igraph and visualized in Cytoscape software[63]. The co-occurrence network node centrality was implemented based on the closeness of nodes and feature vectors. Each node represented a protein gene, while edges represented associations between nodes.

Bacterial growth curve quantification

The frozen *S. oralis* was cultured 1:100 in TSB medium and grown overnight at 37 °C. Then they were transferred to fresh TSB medium, diluted to an absorbance (OD_{600}) of 0.1, and shaken at 220 rpm in a 37 °C shaker. 100 µL of the bacterial solution was added to 96-well plates, and the absorbance (OD_{600}) was tested at 0, 0.5, 1, 2, 4, 8, 12, and 24 h. Three replicates were performed at each time point to quantify the growth curve of *S. oralis* and to fit the curve. Meanwhile, the bacterial solution was coated on TSB agar plates diluted with PBS to calculate the bacterial density.

Biofilm growth curves were measured after adding *S. oralis* ($OD_{600} = 0.1$) to a 24-well plate containing coverslips and incubating at 37 °C for 1, 2, 4, 8, 12, and 24 h. The biofilms were fixed with 2.5% glutaraldehyde. After fixation at room temperature for 2 h, 10% crystal violet was added to the wells for 15 min for staining. After removing the supernatant, the biofilms were decolorized for 15 min, and the absorbance (OD_{595}) of the decolorized solution was measured to quantify the content of the biofilm.

SEM photography

The biofilms were fixed with 2.5% glutaraldehyde at 4 °C overnight. After dehydration with a gradient ethanol series, the samples were performed critical point drying and gold spraying. The biofilm samples were subsequently photographed and analyzed with a field emission scanning electron microscope (Zeiss, SIGMA).

Biofilm quantification by fluorescence microscopy

Overnight cultures of *S. oralis* were diluted to appropriate absorbance ($OD_{600} = 0.1$) and incubated in confocal dishes at 37 °C for 1 h. After fixation with 2.5% glutaraldehyde, 5 µM of DiI membrane fluorescent dye (Yeasen) was added to the culture and stained at 37 °C for 30 min protected from light. The supernatant was gently discarded, and the biofilm was repeatedly washed with PBS to remove the unbound dye. The biofilms were then photographed with CLSM (Leica Stellaris 5 WLL), and the fluorescence intensity of the biofilms was quantified using ImageJ.

Bacterial movement tracking

S. oralis was stained with 5 µM of DiI dye for 30 min at 37 °C protected from light, and then washed with PBS to remove the unbound dye. *S. oralis* was then resuspended with TSB medium and added to the confocal dishes. It was immediately photographed with a Nikon Ti2-E fluorescence microscope for 10 min without a time delay interval. The time interval between photographs was set to 0.22 s. The individual bacterial movement trajectories in the video were analyzed using a MATLAB program to calculate their relevant movement parameters such as MSD, G-Probability, and displacement frequencies. GraphPad Prism 8.0 and Origin 2020 were used for graphical analysis.

Protein movement tracking

The purified protein was diluted to 4 mg mL^{-1}, and 5-Fluorescein isothiocyanate (FITC, Yeasen) at a final concentration of 1 mg/mL was added to 100 µL of protein solution and incubated at 4 °C for 8 h. At the end of the reaction, 50 mM NH_4Cl was added to the solution and reacted for 2 h to terminate the reaction. To remove unbound FITC and obtain a fluorescence-linked protein solution, the reaction solution was centrifuged in a 10 kDa ultrafiltration tube (Millipore) at 5000 rpm for 30 min at 4 °C. The solution was lyophilized at −80 °C.

The protein-FITC was diluted to the appropriate concentration and added dropwise to the coverslips[64]. The motion of individual proteins was tracked by TIRFM, and a video was taken for 10 min. GraphPad Prism 8.0 and Origin 2020 were used for graphical analysis.

Computer theoretical calculations

The GROMACS 2019.2 package, using the charmm36 force field, was used for the molecular dynamics simulations. The 3D structures of EF-Tu (AlphaFoldDB: P33170), Enolase (AlphaFoldDB: A0A428I769), and fibronectin (AlphaFoldDB: P02751) were obtained from the UniProt website. The HA plane was constructed by CHARMM-GUI using the corresponding CHARMM force field. EF-Tu was placed inside the box with the target protein and HA plane to form the system so that the system was 1.5 nm away from the box axis. Water and ions were added to the box for energy minimization. Subsequently, NVT, NPT equilibration, and finally, molecular dynamics simulations were performed for 10 ns. The simulation results were visualized by VMD software the final system was analyzed for equilibrium by RMSD analysis, and the potential energy of amino acid residues was calculated for EF-Tu.

MicroScale thermophoresis (MST) analysis

Enolase and fibronectin proteins were fluorescently labeled using rhodamine dissolved in the buffer (20 mM Hepes, 100 mM NaCl, pH 7.5). For MST measurements, purified EF-Tu protein and BSA protein were subjected to a dilution series of 16 serial 1:1 dilutions with ligand buffer (20 mM Tris–HCl, 100 mM NaCl, pH 7.5). Enolase-Rhodamine and fibronectin-Rhodamine proteins were diluted to the appropriate concentration and incubated with the prepared ligand solution 1:1 for 10 min. Samples were loaded into glass capillaries (NanoTemper Technologies), and microthermophoresis was performed using a 60% LED power supply and high MST power. Dissociation constants (K_d) were calculated from duplicate measured readings via NanoTemper Technologies software.

Periodontitis mouse model

8-week-old C57BL/6 female mice were selected for periodontitis animal modeling. All experiments were approved by the Animal Research Committee of the School of Stomatology, Wuhan University, China. After anesthesia, 5-0 filaments were ligated to the cervical region of the bilateral maxillary second molars of the mice. Overnight cultures of *S. oralis* were diluted to the absorbance (OD_{600}) of 0.1, and 10 µL of the fresh bacterial solution was dropped on the ligature once daily. To observe the role of the tuf gene of *S.oralis* in the pathogenesis of periodontitis, Δ*tuf*, *pDL278tuf*Δ*tuf*, and WT strains were used to coat the ligature lines in the cervical region of the teeth, and the ligated-only group served as a control group. Mice were euthanized 5 days after modeling and subsequent testing was performed. No significant alveolar bone resorption was observed in the ligation-only group at 5 days, and the effect of the tuf gene of *S.oralis* on alveolar bone resorption could be more clearly observed. To observe the effect of simeprevir, 1 µM final concentration of simeprevir was added to the ligature with or without bacterial solutions. The process was repeated for 7 days once a day. To observe the preventive effect of simeprevir on periodontitis in a mouse model of flora transplantation, subgingival plaque from patients with periodontitis was collected and cultured. In the bacterial infection group, the cultured mixed flora was added dropwise to the ligature. In the Simeprevir group, a 1 µM final concentration of simeprevir with or without mixed flora was added dropwise to the ligature, and the ligated-only group served as a control. The mice were euthanized after 7 days of once-daily repeats. To observe the supplementary therapeutic effects of simeprevir on periodontitis in mouse models of colony transplantation, the mouse model of periodontitis that had been ligated was first established, and the ligature was removed on day 7. The procedure with simeprevir and mixed flora solutions was repeated once a day for 7 days. Mice were euthanized on day 14 of the models. Finally, the bilateral maxillary alveolar bone was taken for micro-CT scanning and histological analysis.

Micro-CT and histological analysis

Maxillary alveolar bone was fixed with 4% paraformaldehyde at 4 °C for 48 h and then flushed overnight. The alveolar bone tissue was scanned with a high-resolution micro-computed tomography scanner (SkyScan) with parameters set to 55 kV, 200 µA, and a resolution of 5 µm/pixel. The second molar inter-root alveolar bone was selected as the region of interest (ROI). The reconstructed images were analyzed with CTAn (Bruker), including trabecular bone volume per tissue volume (BV/TV) and trabecular number (Tb. *N*).

The bone tissues were treated with 10% EDTA decalcification solution for 4 weeks to complete decalcification, dehydrated in an ethanol gradient, and then embedded in paraffin. The embedded tissues were cut into 5 μm-thick sections. The sections were then dewaxed and processed for HE (Solarbio) staining and TRAP (Solarbio) staining. Neutral gum was used to seal the sections.

For immunofluorescence experiments, the sections were digested with gastric enzymes. Then, non-specific antigens were blocked with goat serum. The relevant tissues were labeled with rabbit anti-iNOS and rabbit anti-MPO antibody solutions and incubated at 4 °C overnight. Following incubation, the tissues were treated with F4/80-FITC, Ly6G-FITC fluorescent antibody solution, and goat anti-rabbit DyLight 594 fluorescent secondary antibody solution. The tissues were then incubated in a 37 °C incubator for 1 h. After washing away the unconjugated fluorescent antibody with PBS, DAPI fluorescent sealer was added dropwise. Finally, the coverslips were placed and stored at 4 °C.

The sections were photographed with a scanning microscope (Leica, Aperio VERSA 8). Alveolar bone resorption and osteoclast infiltration were analyzed using ImageScope and ImageJ.

Immunotransmission electron microscopy photography

The sample was centrifuged to collect the precipitate and then resuspended and fixed for 2 h at 4 °C with the electron microscope fixative (Servicebio, G1102). The sample was centrifuged again and washed for 3 min with 0.1 M phosphate buffer PB (pH 7.4). A 1% agarose solution, which had been heated and dissolved in advance, was added to the EP tube after cooling. The precipitate was picked up with forceps and wrapped in agarose before it solidified. The agar block was added with 1% osmium tetroxide (Ted Pella Inc.) in 0.1 M phosphate buffer PB (pH 7.4) and fixed for 2 h at room temperature away from light. The supernatant was discarded, and the samples were rinsed 3 times with 0.1 M phosphate buffer PB (pH 7.4) for 15 min each time. The tissues were sequentially dehydrated in 30%–50%–70%–80%–95%–100%–100% alcohol for 20 min each time and finally immersed in 100% acetone twice for 15 min each time. The samples were permeated with the mix at 37 °C for 2–4 h, which contained acetone (Sinaopharm Group Chemical Reagent Co., Ltd, 10000418): 812 embedding agents (SPI, 90529-77-4) = 1:1. Next, the samples were treated with the mix with acetone: 812 embedding agents = 1:2 at 37 °C overnight. Subsequently, pure 812 embedding agents were used for 5–8 h at 37 °C. The pure 812 embedding agents were poured into the embedding plate, and the samples were inserted into the plate and placed in the oven at 37 °C overnight. The plates were then polymerized in an oven at 60 °C for 48 h, and the resin blocks were removed and set aside.

The tissue blocks were cut into ultrathin sections of 60–80 nm using an ultrathin sectioning machine (Leica, Leica UC7), and the slices were retrieved with a 150-mesh copper mesh with Formvar films. The copper mesh was stained in a 2% uranyl acetate saturated alcohol solution for 8 min away from light. After staining, the slices were sequentially washed 3 times with 70% alcohol and 3 times with ultrapure water. The copper mesh was then stained with 2.6% lead citrate solution for 8 min away from carbon dioxide. The slices were washed 3 times with ultrapure water and blotted slightly on filter paper. Copper mesh sections were placed in a copper mesh box and dried overnight at room temperature. The sections were observed under a transmission electron microscope (Hitachi, HT7800/HT7700), and images were collected.

MV extraction

An appropriate amount of overnight *S. oralis* was diluted to 8 L with TSB medium, added to several Petri dishes, and placed in a 37 °C incubator for 1 h. The supernatant was discarded, and the biofilm was resuspended in PBS. The collected bacterial broth was centrifuged at 10,000 rpm for 5 min to obtain the supernatant. The supernatant was sequentially passed through 0.45 and 0.22 μm filters (Millipore) to remove the bacteria and retain the liquid-containing vesicles. The supernatant was added to a 100 kDa ultra-filtration tube (Millipore) and centrifuged at 4 °C, 5000 rpm for

concentration. Subsequently, the MV precipitates were obtained by centrifugation at 150,000 rpm for 3 h in an ultra-high-speed frozen centrifuge (Beckman). Protein concentration was measured using a BCA Protein Quantification Kit (Vazyme).

Pull-down assay

S. oralis with pDL278-*tuf*-his-tag and pDL278-*eno*-his-tag were centrifuged to collect the precipitate. SMM Buffer (0.02 M maleic acid, 0.5 M sucrose, and 0.02 M MgCl$_2$) containing 5 mg/mL lysozyme (Biosharp) was prepared and supplemented with phenylmethylsulfonylfluoride (PMSF). The bacterial precipitate was resuspended with SMM Buffer and shaken at 37 °C, 220 rpm for 30 min in a shaker. The bacterial suspension was centrifuged at 4 °C, 6000 rpm for 5 min, and the supernatant was removed. The precipitate was repeatedly washed with PBS to remove the lysozyme. The bacteria precipitates were resuspended with an appropriate amount of SMM Buffer containing PMSF and sonicated on ice for 3 h until the suspension was clarified. The supernatant was collected after centrifugation and filtered with the 0.22 μm filters. The MVs were stored at −80 °C.

For the purified protein pull-down assay, the purified protein was diluted to 4 mg mL^{-1} and mixed in equal amounts. To characterize the inhibitory effect of simeprevir, 1 μM of simeprevir was added to the mixed protein solution.

An appropriate amount of magnetic beads was prepared by taking 30 μL of each sample and washing several times with Binding Buffer according to the commercial instructions of Protein A (or A/G) Immunoprecipitation Kit (Beaver Biosciences). The magnetic beads were resuspended with 1 mL of Binding Buffer, added with 30 μL of His-Tag antibody (ABclonal), and mixed on a shaker for 30 min at room temperature. The supernatant was discarded, and the unbound antibody was removed by washing several times with Binding Buffer. The pretreated beads were added to the samples and shaken overnight at 4 °C. After discarding the supernatant, the beads were washed several times with Washing Buffer, and the proteins on the beads were extracted with 100 μL of Elution Buffer. The mixture was added to a final concentration of 1×SDS protein loading buffer (Biosharp) and boiled at 98 °C for 10 min. The protein supernatant was collected and stored at −80 °C.

Western blotting

A final concentration of 1×SDS protein loading buffer was added to the samples, and protein denaturation was completed at 98 °C. The denatured proteins were performed to electrophoresis and transferred to PVDF (Roche) membranes. After washing with Tris-buffered saline Tween (TBST), the membranes were blocked with QuickBlock Blocking Buffer (Beyotime) for 15 min at room temperature on a shaker. The membranes were incubated with 1:1000 Rabbit anti-Flag-Tag antibody (MBL) at 4 °C overnight. The membranes were washed with TBST and incubated with 1:8000 Goat Anti-Rabbit IgG (H + L) antibody (ABclonal) for 1 h at room temperature on a shaker. After washing with TBST, the signal of Enoalse-Flag was detected with the Super-sensitive ECL chemiluminescent substrate (Biosharp). Subsequently, the membranes were washed with TBST and treated with Stripping Buffer (CWBio) for 10 min in a room-temperature shaker. After washing off the supernatant with TBST, the membranes were blocked with QuickBlock Blocking Buffer at room temperature and incubated with 1:1000 Mouse anti-His-Tag antibody (ABclonal) at 4 °C overnight, and the protein signal of EF-Tu-His was detected. The Western Blot results were quantified using ImageJ.

Oral plaque clinical trials

Twelve healthy oral volunteers who met the criteria were screened and divided equally into 2 groups of 6 each, one group for dynamic testing of the effect of simeprevir mouthwash on oral plaque growth and one group for plaque testing of the effect of simeprevir mouthwash on assisted toothbrushing. For the dynamic test group of the effect of simeprevir mouthwash on oral plaque growth, the volunteers were first cleaned with oral hygiene to remove plaque. Volunteers were gargled with 1 μM of simeprevir

mouthwash for 30 s and were prohibited from brushing their teeth during the test period. The plaque staining was performed with a plaque indicator at 1, 2, 4, 6, 8 h after rinsing, and the Quigley–Hein plaque index was counted and photographed. The 6 volunteers were divided into 2 groups of 3 each again, and the subgingival plaques of 9 dental sites were collected with probes at 24 and 48 h, respectively, for measuring the bacterial density with plate counting. Similar to the above procedure, volunteers rinsed their mouths with double-distilled water and then performed their own control experiment. For the plaque test group of the effect of simeprevir mouthwash on assisted brushing, volunteers were first given an oral hygiene cleaning to remove plaque. The volunteers brushed their teeth twice a day during the test period and rinsed 1 μM of simeprevir mouthwash for 30 sec after brushing. Plaque staining with plaque indicator was performed on day 1, day 3, day 5, and day 7, and the Quigley–Hein plaque index was counted, photographed, and recorded. Similar to the above procedure, volunteers rinsed their mouths with double-distilled water and then performed their own control experiment.

Statistical analysis

Statistical significance was assessed by appropriate tests (see figure legends). Analysis was performed using GraphPad Prism 8.0, and $P < 0.05$ was considered significant. The unpaired t-test, One-way ANOVA, and Two-way ANOVA were used, and the asterisks indicate the level of significance: $*P < 0.05$, $**P < 0.01$, $***P < 0.001$. No statistical methods were used to predetermine the sample size, and the researchers were not blinded to the allocation during the experiment and outcome assessment. No data were excluded from the analysis.

Data availability

The raw metagenomic sequencing data are available in the NCBI SRA database under the primary accession codes PRJNA396840 and PRJNA678453. Source data for this study are available upon request from the corresponding author.

Code availability

No original code was used in this study. All data analysis was performed using publicly available software/tools.

References

1. Albandar, J. M., Brunelle, J. A. & Kingman, A. Destructive periodontal disease in adults 30 years of age and older in the United States, 1988–1994. *J. Periodontol.* **70**, 13–29 (1999).
2. Dye, B. A. et al. Trends in oral health status: United States, 1988–1994 and 1999–2004. *Natl Cent. Health Stat.* **11**, 248 (2007).
3. Czesnikiewicz-Guzik, M. et al. Causal association between periodontitis and hypertension: evidence from Mendelian randomization and a randomized controlled trial of non-surgical periodontal therapy. *Eur. Heart J.* **40**, 3459–3470 (2019).
4. D'Aiuto, F. et al. Systemic effects of periodontitis treatment in patients with type 2 diabetes: a 12 month, single-centre, investigator-masked, randomised trial. *Lancet Diabetes Endocrinol.* **6**, 954–965 (2018).
5. Engebretson, S. P. et al. The effect of nonsurgical periodontal therapy on hemoglobin A1c levels in persons with type 2 diabetes and chronic periodontitis: a randomized clinical trial. *JAMA* **310**, 2523–2532 (2013).
6. Hajishengallis, G. & Chavakis, T. Local and systemic mechanisms linking periodontal disease and inflammatory comorbidities. *Nat. Rev. Immunol.* **21**, 426–440 (2021).
7. Jungbauer, G. et al. Periodontal microorganisms and Alzheimer disease—a causative relationship? *Periodontology 2000* **89**, 59–82 (2022).
8. Nwizu, N., Wactawski-Wende, J. & Genco, R. J. Periodontal disease and cancer: epidemiologic studies and possible mechanisms. *Periodontology 2000* **83**, 213–233 (2020).
9. Orlandi, M., Graziani, F. & D'Aiuto, F. Periodontal therapy and cardiovascular risk. *Periodontology 2000* **83**, 107–124 (2020).
10. Dominy, S. S. et al. Porphyromonas gingivalis in Alzheimer's disease brains: evidence for disease causation and treatment with small-molecule inhibitors. *Sci. Adv.* **5**, eaau3333 (2019).
11. Kinane, D. F., Stathopoulou, P. G. & Papapanou, P. N. Periodontal diseases. *Nat. Rev. Dis. Prim.* **3**, 17038 (2017).
12. Krishna, R. & De Stefano, J. A. Ultrasonic vs. hand instrumentation in periodontal therapy: clinical outcomes. *Periodontology 2000* **71**, 113–127 (2016).
13. Graziani, F. et al. Nonsurgical and surgical treatment of periodontitis: how many options for one disease? *Periodontology 2000* **75**, 152–188 (2017).
14. Yang, R. et al. The regulatory effect of coaggregation between *Fusobacterium nucleatum* and *Streptococcus gordonii* on the synergistic virulence to human gingival epithelial cells. *Front. Cell. Infect. Microbiol.* **12**, 879423 (2022).
15. Whitmore, S. E. & Lamont, R. J. The pathogenic persona of community-associated oral *Streptococci*. *Mol. Microbiol.* **81**, 305–314 (2011).
16. Metzger, Z. et al. Characterization of coaggregation of *Fusobacterium nucleatum* PK1594 with six *Porphyromonas gingivalis* strains. *J. Endod.* **35**, 50–54 (2009).
17. Metzger, Z. et al. Synergistic pathogenicity of *Porphyromonas gingivalis* and *Fusobacterium nucleatum* in the mouse subcutaneous chamber model. *J. Endod.* **35**, 86–94 (2009).
18. Ali Mohammed, M. M. et al. Characterization of extracellular polymeric matrix, and treatment of *Fusobacterium nucleatum* and *Porphyromonas gingivalis* biofilms with DNase I and proteinase K. *J. Oral Microbiol.* **5**, (2013).
19. Saito, A. et al. Fusobacterium nucleatum enhances invasion of human gingival epithelial and aortic endothelial cells by *Porphyromonas gingivalis*. *FEMS Immunol. Med. Microbiol.* **54**, 349–355 (2008).
20. Wright, C. J. et al. Microbial interactions in building of communities. *Mol. Oral Microbiol.* **28**, 83–101 (2012).
21. Chen, Y., Li, Y. & Zou, J. Intrageneric and intergeneric interactions developed by oral Streptococci: pivotal role in the pathogenesis of oral diseases. *Curr. Issues Mol. Biol.* **32**, 377–434 (2019).
22. Merritt, J. & Qi, F. The mutacins of *Streptococcus mutans*: regulation and ecology. *Mol. Oral Microbiol.* **27**, 57–69 (2011).
23. Back, C. R. et al. *Streptococcus gordonii* DL1 adhesin SspB V-region mediates coaggregation via receptor polysaccharide of *Actinomyces oris* T14V. *Mol. Oral Microbiol.* **30**, 411–424 (2015).
24. Bensing, B. A. et al. Novel aspects of sialoglycan recognition by the Siglec-like domains of streptococcal SRR glycoproteins. *Glycobiology* **26**, 1222–1234 (2016).
25. Abranches, J. et al. Biology of oral Streptococci. *Microbiol. Spectr.* **6**, 5 (2018).
26. Bowen, W. H. Dental caries—not just holes in teeth! A perspective. *Mol. Oral Microbiol.* **31**, 228–233 (2015).
27. Robinson, M. W. et al. MHJ_0125 is an M42 glutamyl aminopeptidase that moonlights as a multifunctional adhesin on the surface of *Mycoplasma hyopneumoniae*. *Open Biol.* **3**, 130017 (2013).
28. Balish, M. F. et al. Subunits of the pyruvate dehydrogenase cluster of *Mycoplasma pneumoniae* are surface-displayed proteins that bind and activate human plasminogen. *PLoS ONE* **10**, e0126600 (2015).
29. Pinto, P. M. et al. Proteomic survey of the pathogenic *Mycoplasma hyopneumoniae* strain 7448 and identification of novel post-translationally modified and antigenic proteins. *Vet. Microbiol.* **121**, 83–93 (2007).
30. Ariga, H. et al. Immunoproteomic to analysis the pathogenicity factors in leukopenia caused by *Klebsiella pneumoniae* bacteremia. *PLoS ONE* **9**, e110011 (2014).
31. Mirzaei, R. et al. Identification of proteins derived from *Listeria monocytogenes* inducing human dendritic cell maturation. *Tumor Biol.* **37**, 10893–10907 (2016).

32. Cowles, K. N. & Gitai, Z. Surface association and the MreB cytoskeleton regulate pilus production, localization and function in *Pseudomonas aeruginosa*. *Mol. Microbiol.* **76**, 1411–1426 (2010).

33. Isberg, R. R. et al. A novel system of cytoskeletal elements in the human pathogen *Helicobacter pylori*. *PLoS Pathog.* **5**, e1000669 (2009).

34. Kolenbrander, P. E. et al. Oral multispecies biofilm development and the key role of cell–cell distance. *Nat. Rev. Microbiol.* **8**, 471–480 (2010).

35. Yan, F. et al. Isolation, purification, gene cloning and expression of antifungal protein from *Bacillus amyloliquefaciens* MG-3. *Food Chem.* **349**, 129130 (2021).

36. de Amo, G. S. et al. Heterologous expression, purification and biochemical characterization of a new xylanase from *Myceliophthora heterothallica* F.2.1.4. *Int. J. Biol. Macromol.* **131**, 798–805 (2019).

37. Tanner, A. C. R. et al. Subgingival and tongue microbiota during early periodontitis. *J. Dent. Res.* **85**, 318–323 (2006).

38. Lu, J. et al. Periodontitis-related salivary microbiota aggravates Alzheimer's disease via gut–brain axis crosstalk. *Gut Microbes* **14**, 2126272 (2022).

39. Enersen, M., Nakano, K. & Amano, A. *Porphyromonas gingivalis* fimbriae. *J. Oral Microbiol.* **5**, (2013).

40. Wright, C. J. et al. Characterization of a bacterial tyrosine kinase in Porphyromonas gingivalis involved in polymicrobial synergy. *MicrobiologyOpen* **3**, 383–394 (2014).

41. Morillo-Lopez, V. et al. Corncob structures in dental plaque reveal microhabitat taxon specificity. *Microbiome* **10**, 145 (2022).

42. Gholizadeh, P. et al. Oral pathogenesis of *Aggregatibacter actinomycetemcomitans*. *Microb. Pathog.* **113**, 303–311 (2017).

43. Stacy, A. et al. Bacterial fight-and-flight responses enhance virulence in a polymicrobial infection. *Proc. Natl Acad. Sci. USA* **111**, 7819–7824 (2014).

44. Stacy, A. et al. The biogeography of polymicrobial infection. *Nat. Rev. Microbiol.* **14**, 93–105 (2015).

45. Balbo, M. et al. Infection of human B lymphoma cells by *Mycoplasma fermentans* induces interaction of its elongation factor with the intracytoplasmic domain of Epstein-Barr virus receptor (gp140, EBV/C3dR, CR2, CD21). *FEMS Microbiol. Lett.* **249**, 359–366 (2005).

46. O'Connor, T. M. et al. The role of substance P in inflammatory disease. *J. Cell. Physiol.* **201**, 167–180 (2004).

47. Amendola, R. et al. Effects of a skin neuropeptide (substance P) on cutaneous microflora. *PLoS ONE* **8**, e78773 (2013).

48. N'Diaye, A. et al. Effect of substance P in *Staphylococcus aureus* and *Staphylococcus epidermidis* virulence: implication for skin homeostasis. *Front. Microbiol.* **7**, 506 (2016).

49. Widjaja, M. et al. Elongation factor Tu is a multifunctional and processed moonlighting protein. *Sci. Rep.* **7**, 11227 (2017).

50. Brookes, Z. et al. Mouthwash effects on the oral microbiome: are they good, bad, or balanced? *Int. Dent. J.* **73**, S74–S81 (2023).

51. Tang, W. et al. Expression, purification and identification of recombinant mouse interleukin 21 protein in *E. coli*. *Cell. Mol. Immunol.* **3**, 311–315 (2006).

52. Berlanga-Clavero, M. V. et al. Bacillus subtilis biofilm matrix components target seed oil bodies to promote growth and anti-fungal resistance in melon. *Nat. Microbiol.* **7**, 1001–1015 (2022).

53. McIver, L. J. et al. bioBakery: a meta'omic analysis environment. *Bioinformatics* **34**, 1235–1237 (2018).

54. Beghini, F., et al. Integrating taxonomic, functional, and strain-level profiling of diverse microbial communities with bioBakery 3. *Elife* **10**, (2021).

55. Hadley, W. *ggplot2 Elegant Graphics for Data Analysis* (ed. Parmigiani, R.G.K.H.G.) (Springer, 2016).

56. Harrower, M. & Brewer, C. A. ColorBrewer.org: an online tool for selecting colour schemes for maps. *Cartogr. J.* **40**, 27–37 (2003).

57. Ahlmann-Eltze, C. & Patil, I. *ggsignif: R Package for Displaying Significance Brackets for 'ggplot2'*. Preprint at: https://doi.org/10.31234/osf.io/7awm6 (2021).

58. Love, M. I., Huber, W. & Anders, S. Moderated estimation of fold change and dispersion for RNA-seq data with DESeq2. *Genome Biol.* **15**, 550 (2014).

59. Oksanen, J. et al. *Community Ecology Package.* Preprint at: https://github.com/vegandevs/vegan (2022).

60. Sun, Y., Hurlimann, S. & Garner, E. Growth rate is modulated by monitoring cell wall precursors in *Bacillus subtilis*. *Nat. Microbiol.* **8**, 469–480 (2023).

61. Kanehisa, M. et al. KEGG: new perspectives on genomes, pathways, diseases and drugs. *Nucleic Acids Res.* **45**, D353–D361 (2017).

62. Bu, D. et al. KOBAS-i: intelligent prioritization and exploratory visualization of biological functions for gene enrichment analysis. *Nucleic Acids Res.* **49**, W317–W325 (2021).

63. Shannon, P. et al. Cytoscape: a software environment for integrated models of biomolecular interaction networks. *Genome Res.* **13**, 2498–2504 (2003).

64. Zhou, J. et al. Deoxygenated hydroxyapatite inhibits macrophage inflammation through fibronectin restricted adsorption. *Acta Biomater.* **191**, 177–188 (2025).

Acknowledgements

Author contributions

Leyi Xiao: Conceptualization, resources, data curation, formal analysis, validation, investigation, visualization, methodology, and writing—original draft; project administration. Yingying Pu: Conceptualization, formal analysis, investigation, methodology, writing—review and editing. Yu Cui: Resources, formal analysis, methodology, investigation, visualization, and writing—review and editing. Chen Chen: Resources, formal analysis, and methodology. Qi Xiao: Resources, formal analysis, and methodology. Yulan Wang: Conceptualization, validation, project administration, and writing—review and editing. Yan Wei: Resources, visualization, and methodology. Mengge Feng: Resources, visualization, and methodology. Tiange Zhang: Resources, formal analysis, methodology, and visualization. Shanyi Yang: Resources, formal analysis, methodology, and visualization. Jingxuan Zhou: Resources, formal analysis, and methodology. Jinglun Zhang: Resources and methodology. Yueqi Ni: Resources and methodology. Hebin Liao: Resources, formal analysis, and methodology. Jingwen Wu: Resources and formal analysis.

Competing interests

The authors declare no competing interests.

Additional information

Publisher's note Springer Nature remains neutral with regard to jurisdictional claims in published maps and institutional affiliations.